The Astrophysical Journal, 883:137 (10pp), 2019 October 1 https://doi.org/10.3847/1538-4357/ab3afa

Two-zone Emission Modeling of PKS 1510-089 during the High State of 2015

Raj Prince[1], Nayantara Gupta[1], and Krzysztof Nalewajko[2]
[1] Raman Research Institute, C.V. Raman Avenue, Sadashivanagar, Bangalore 560080, India; rajprince@rri.res.in
[2] Nicolaus Copernicus Astronomical Center, Polish Academy of Sciences, Bartycka 18, 00-716 Warsaw, Poland
Received 2019 May 6; revised 2019 August 8; accepted 2019 August 12; published 2019 September 27

Abstract

PKS 1510-089 is one of the most variable blazars in the third *Fermi*-LAT source catalog. During 2015, this source has shown four flares identified as flares A, B, C, and D in between three quiescent states: Q1, Q2, and Q3. The multiwavelength data from *Fermi*-LAT, *Swift*-XRT/Ultraviolet/Optical Telescope, Owens Valley Radio Observatory, and Sub-millimeter array Observatory are used in our work to model these states. Different flux doubling times have been observed in different energy bands, which indicate that there could be multiple emission zones. The flux doubling time from the gamma-ray and X-ray light curves are found to be 10.6 hr, 2.5 days, and the average flux doubling time in the optical/UV band is 1 day. It is possible that the gamma-ray and optical/UV emission are produced in the same region whereas X-ray emission is coming from a different region along the jet axis. We have also estimated the discrete correlation functions (DCFs) among the light curves of different energy bands to infer about their emission regions. However, our DCF analysis does not show significant correlation in different energy bands though it shows peaks in some cases at small time lags. We perform a two-zone multiwavelength time-dependent modeling with one emission zone located near the outer edge of the broad line region and another further away in the dusty/molecular torus (DT/MT) region to study this high state.

Key words: galaxies: active – galaxies: jets – gamma rays: galaxies – quasars: individual (PKS 1510-089)

Supporting material: data behind figure

1. Introduction

Being one of the most variable flat spectrum radio quasars (FSRQs) in the third *Fermi*-LAT source catalog (3FGL) PKS 1510-089 has been well observed during its high states in the past. It is located at a redshift of $z = 0.361$ (Tanner et al. 1996) with black hole mass $5.4 \times 10^8\ M_\odot$ and accretion rate approximately $0.5\ M_\odot\ \mathrm{yr}^{-1}$ (Abdo et al. 2010). A long-term analysis of the light curve of PKS 1510-089 with the eight year *Fermi*-LAT data has been done by Prince et al. (2017) earlier. They have observed five major flares during 2008–2016, and their temporal and spectral features have been studied in detail. During its high activity period between 2008 September and 2009 June its gamma-ray emission showed a weak correlation with the UV, strong correlation with the optical and no correlation with the X-ray emission (Abdo et al. 2010). PKS 1510-089 was also studied by Nalewajko (2013), where he used the first four years of *Fermi*-LAT data and observed 14 flares with a minimum and maximum flux of 7.4 and 26.6 $(\times 10^{-6})\ \mathrm{ph\ cm^{-2}\ s^{-1}}$, respectively. Detection of high energy gamma-rays up to 300–400 GeV has been reported by the H.E.S.S. collaboration (Abramowski et al. 2013) during 2009 March–April and by the MAGIC collaboration (Aleksić et al. 2014) between 2012 February 3 and April 3.

In the second half of 2011 this source was active in several energy bands and the optical, gamma-ray, and radio flares were detected. The gamma-ray variability down to 20 minutes indicated the highly variable nature of this source. Aleksić et al. (2014) did a detailed multiwavelength modeling for the period 2012 January–April covering radio to very high energy gamma-rays. They explained the multiwavelength emission as the result of turbulent plasma flowing at a relativistic speed down the jet and crossing a standing conical shock. In modeling the spectral energy distributions (SEDs) from PKS 1510-089 it is most commonly thought that the low energy (radio, optical) emission is from synchrotron radiation of relativistic electrons and high energy emission (X-ray, gamma-ray) is from external Compton (EC) scattering of the seed photons in the broad line region (BLR) and dusty torus (DT) region (Kataoka et al. 2008; Abdo et al. 2010; Brown 2013; Barnacka et al. 2014). The gamma-ray emission region could also be located at a radio knot, far away from the black hole as suggested by Marscher et al. (2010). They modeled the eight major gamma-ray flares of PKS 1510-089 that happened in 2009. During optical and gamma-ray flares a bright radio knot traveled through the core/stationary feature at 43 GHz seen by VLBA (Very Long Baseline Array) images. The knot continued to propagate down the length of the jet at an apparent speed of 22 c. A strong emission in gamma-ray energy accompanied by a month long emission in X-ray/radio emission, which gradually intensified, represented the complex nature of the flares.

The hadronic scenario of high energy photon emission (X-ray, gamma-ray) by p–γ interactions and proton synchrotron emission has been studied before (Böttcher et al. 2013; Basumallick & Gupta 2016). Hadronic models require super-Eddington luminosities to explain the gamma-ray flux.

A two zone modeling was considered earlier by Nalewajko et al. (2012) after including Herschel observations, *Fermi*-LAT, *Swift*, SMARTS, and Submillimeter Array data for explaining the spectral and temporal features of activities of PKS 1510-089 in 2011. From 2015 March to August this source was again very active. Optical *R*-band monitoring with ATOM, supporting H.E.S.S. observations, detected very high flux of optical photons (Zacharias et al. 2016).

Its enhanced activity in very high energy gamma-rays was also observed by the MAGIC telescope (Ahnen et al. 2017) in May, 2015. In the middle of a long high state in optical and gamma-rays, for the first time they detected a fast variability in very high energy gamma-rays. Their observation periods MJD

57160-57161 (Period A) and MJD 57164-57166 (Period B) overlap with one of the flares identified as flare-B (MJD 57150-57180) in our work. They collected simultaneous data in radio, optical, UV, X-ray, and gamma-ray frequencies for multi-wavelength modeling. They noted most of the flux variation happened in *Fermi*-LAT and MAGIC energy bands.

The complex nature of multiwavelength emission indicated by a single zone model is not suitable for explaining the flares of PKS 1510-089. In the present work several months of observational data have been studied for multiwavelength modeling of the high state of PKS 1510-089 in 2015.

The paper is organized as follows: in Section 2, we have provided details about the multiwavelength data used in our study. In Section 3, we have presented our results, in Section 4, we have discussed our results and compared with the previous studies on this source.

2. Multiwavelength Data Analysis

The *Fermi*-LAT and *Swift*-XRT/UVOT observations together cover optical, ultraviolet, X-ray and gamma-ray energy bands, which allow us to do multiwavelength variability analysis and modeling of blazar flares.

2.1. Fermi-*LAT*

After the successful launch of the *Fermi Gamma-ray Space Telescope* in 2008, thousands of sources were revealed in the gamma-ray sky by the onboard instrument, Large Area Telescope (LAT), over the past 11 years. With a field of view of about 2.4 sr (Atwood et al. 2009) LAT covers 20% of the sky at any time and scans the whole sky every three hours. It is sensitive to photons having energy between 20 MeV to higher than 500 GeV. The third *Fermi* source catalog (3FGL; Acero et al. 2015) shows that the extragalactic sky is dominated by active galactic nuclei emitting high energy gamma-rays. The FSRQ PKS 1510-089 has been continuously monitored by *Fermi*-LAT since 2008 August. We collected the data for the year 2015 and analyzed it for energy range 0.1–300 GeV. A circular region of radius 10° is chosen around the source of interest and the circular region is known as the region of interest (ROI). The detailed procedure to analyze the *Fermi*-LAT data is given in Prince et al. (2018).

The data analysis also takes care of contamination from Earth's limb gamma-rays by rejecting the events having zenith angle higher than 90°. In this analysis, we have used the latest instrument Response Function "P8R2_SOURCE_V6" provided by the *Fermi* Science Tools.

2.2. Swift-*XRT/UVOT*

Swift data for PKS 1510-089 has been collected from the *HEASARC* webpage[3] for a period of one year during 2015, which is part of the archived data. In total 44 observations were reported during 2015. A task *"xrtpipeline"* version 0.13.2 has been run for every observation to get the cleaned event files. The latest version of calibration files (CALDB version 20160609) and standard screening criteria have been used to reprocess the raw data. Cleaned event files corresponding to the Photon Counting mode have been considered for further analysis. A circular region of radius 20″ around the source and away from the source has been chosen for the source and the background, respectively, while analyzing the XRT data. The X-ray light curve and spectra have been extracted by a tool called *xselect*. The spectrum has been obtained and fitted in "xspec"' using a simple power law (PL) model with the galactic absorption column density $n_{\rm H} = 6.89 \times 10^{20}\,{\rm cm}^{-2}$ (Kalberla et al. 2005). The *Swift* Ultraviolet/Optical Telescope (UVOT; Roming et al. 2005) also observed PKS 1510-089 in all six filters *U*, *V*, *B*, *W1*, *M2*, and *W2*. The source image has been extracted by choosing a circular region of 5″ around the source. Similarly, the background region has also been chosen with a radius of 10″ away from the source. The task "uvotsource" has been used to extract the source magnitudes and fluxes. Magnitudes are corrected for galactic extinction ($E(B-V) = 0.087$ mag; Schlafly & Finkbeiner 2011) and converted into a flux using the zero-points (Breeveld et al. 2011) and conversion factors (Larionov et al. 2016).

2.3. Radio Data at 15 and 230 GHz

PKS 1510-089 was also observed in radio wavelength by Owens Valley Radio Observatory (OVRO; Richards et al. 2011)[4] at 15 GHz and by Sub-millimeter array (SMA)[5] at 230 GHz (Gurwell et al. 2007) as a part of the *Fermi* monitoring program. We have collected the data for the year 2015 from both the observatories.

3. Results

In this section, we have presented the results obtained from temporal and spectral analysis, and we have discussed the importance of these results in multiwavelength SED modeling.

3.1. Multiwavelength Light Curves

Multiwavelength light curves are shown in Figure 1, where they show an indication of flares in various wavebands during the year of 2015 for PKS 1510-089.

The topmost panel of Figure 1 represents the gamma-ray light curve. The gamma-ray light curve is divided into different states on the basis of the fluxes observed during different time periods. We have also estimated the fractional rms variability amplitudes (Fossati et al. 2000; Vaughan et al. 2003) to identify the different states. If the value of the fractional variability during a time period is more than 0.5 (50%), then it is considered as a flaring state. During the time period MJD 57023–57100, the average flux of the source is found to be $2.49 \pm 0.10 (\times 10^{-7}\,{\rm ph\,cm^{-2}\,s^{-1}})$ and it does not change significantly. The fractional variability amplitude is found to be 0.50 ± 0.04. This period has been identified as quiescent state Q1.

The source started showing high activity from MJD 57100 and continued for almost 50 days until MJD 57150. The average flux measured during this period is 10.06 ± 0.19 $(\times 10^{-7}\,{\rm ph\,cm^{-2}\,s^{-1}})$, which is five times higher than that in the quiescent state Q1. The fractional variability found during this period is 0.67 ± 0.02, which confirms that the source is more variable than in state Q1. This period is defined as flare A in our Figure 1.

After the end of flare A, in 2–3 days the flux again started rising and it lasted for a month. This period is noted as MJD 57150–57180. The average flux estimated during this period is

[3] https://heasarc.gsfc.nasa.gov/cgi-bin/W3Browse/w3browse.pl

[4] http://www.astro.caltech.edu/ovroblazars/index.php?page=sourcelist

[5] http://sma1.sma.hawaii.edu/callist/callist.html

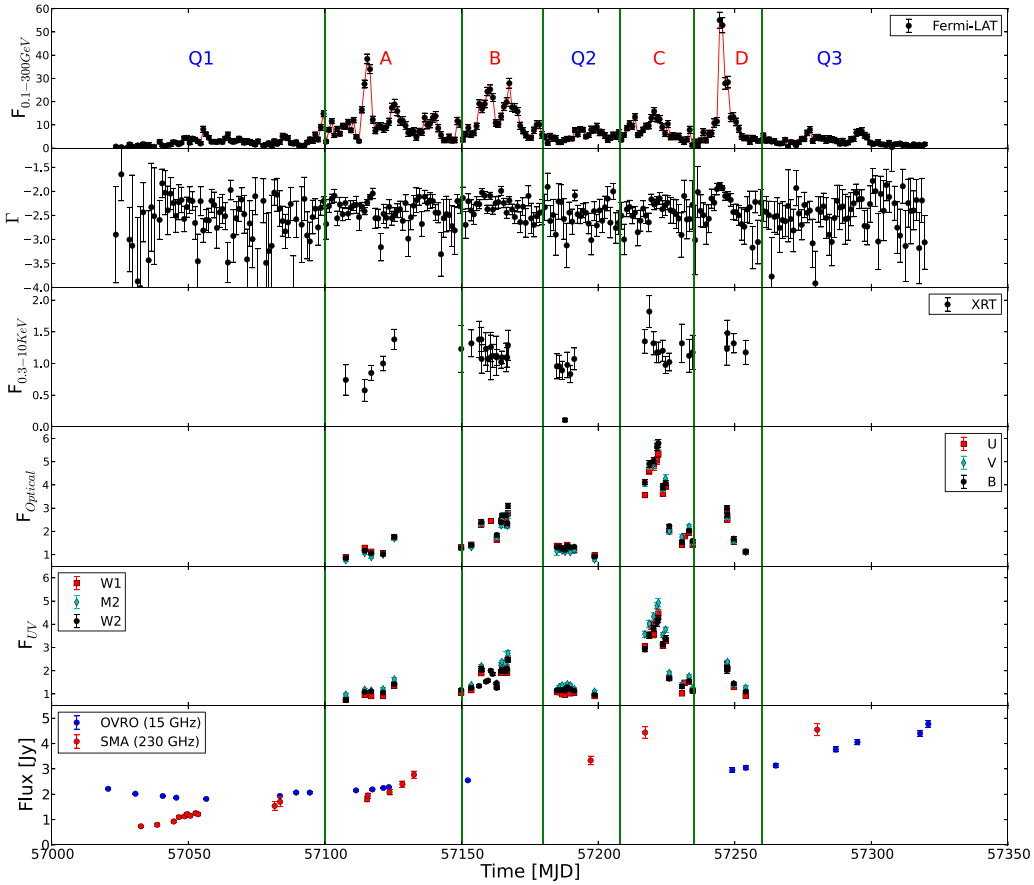

Figure 1. Light curve of PKS 1510-089 during 2015. Four flares A, B, C, and D have been detected with three quiescent states Q1, Q2, and Q3. Vertical green lines separate the different states of the source. Top panel represents the *Fermi*-LAT data for 1 day binning along with corresponding photon spectral index in the second panel. *Swift*-XRT and UVOT light curves are shown in panels 3, 4, and 5. The last panel shows the radio light curve in two different energy bands, 15 and 230 GHz. The γ-ray flux data points are in units of 10^{-7} ph cm^{-2} s^{-1} and X-ray/UV/Optical are in units of 10^{-11} erg cm^{-2} s^{-1}.

(The data used to create this figure are available.)

12.17 ± 0.26 ($\times 10^{-7}$ ph cm^{-2} s^{-1}). The fractional variability measured during this period is 0.57 ± 0.02, which is higher than that in state Q1. This period of high flux and high variability amplitude is referred to as flare B in our work.

After flare B, the source flux became lower compared to flares A and B and the source remained for a month (MJD 57180–57208) in this low state. The average flux obtained during this low state is 5.37 ± 0.21 ($\times 10^{-7}$ ph cm^{-2} s^{-1}) and the fractional variability amplitude measured as 0.28 ± 0.04. The flux variability is not significant during this period as it is below 30%. We have named this period as quiescent state Q2.

During the time period MJD 57208–57235, the source again went to a high state compared to Q1 and Q2, with average flux 7.20 ± 0.23($\times 10^{-7}$ ph cm^{-2} s^{-1}). The flux variability amplitude measured during this period is 0.51 ± 0.03, which is just above the limit we have set (50%). The large average flux and 51% fractional variability suggest that this period is different from states Q1 and Q2. Therefore, this state is identified as flare-C in gamma-rays, which also have a strong flaring counterpart in optical/UV.

A higher state surpassing all the observed flares and quiescent states was observed during the time period MJD 57235–57260. The average flux estimated during this period is 12.67 ± 0.36 ($\times 10^{-7}$ ph cm^{-2} s^{-1}), which is much higher than the average flux observed during any of the other states. A huge flux variation can be seen from Figure 1, and the fractional variability amplitude measured during this period is 1.16 ± 0.03 (>100%). This period of high state is defined as flare D.

After flare D, the flux decreased sharply and attained an average value of 2.93 ± 0.12 ($\times 10^{-7}$ ph cm^{-2} s^{-1}). The source continued to have this average flux over a long period of time from MJD 57260–57320. A small variation in flux was seen during this period (see Figure 1), for which the fractional variability amplitude has been estimated as 0.50 ± 0.05. Since the average flux in this state is very low compare to the flaring states, we have considered this period as quiescent state Q3.

The maximum flux observed during flares A, B, C, and D are 38.4, 27.92, 15.78, and 55.05 ($\times 10^{-7}$ ph cm^{-2} s^{-1}) at MJD 57115.5, 57167.5, 57220.5, and 57244.5 respectively. Flare D has been identified as the brightest gamma-ray flare of the year 2015. In Figure 1, the gamma-ray light curve is binned in one day time bin. The other light curves do not have an equally spaced binning because different observations were carried out at different times. We have estimated the average time between two consecutive observations for X-ray and optical/UV light curves. In X-ray it is found to be 3.4 days and in optical/UV band it is estimated as 4.1, 4.3, 3.8, 3.8, 4.4, and 3.5 days for filters *B*, *V*, *U*, *W1*, *M2*, and *W2* respectively.

Table 1
We Have Scanned All the Light Curves Shown in Figure 1 by Equation (1) and the Flux Doubling Times (τ_d) Are Estimated for All the Different Bands

Telescope/Bands	F_1	F_2	t_1	t_2	τ_d
Fermi-LAT					(hr)
γ-rays	1.15	5.50	57243.5	57244.5	10.6
Swift-XRT/UVOT					(days)
X-rays	1.38	1.07	57156.41	57157.34	2.5
U	2.27	2.78	57166.72	57167.01	1.0
B	2.35	3.09	57166.72	57167.01	0.7
V	2.24	2.70	57166.72	57167.01	1.1
W1	1.91	2.47	57166.72	57167.01	0.8
M2	2.40	2.76	57166.72	57167.01	1.4
W2	2.07	2.47	57166.72	57167.01	1.1

Note. The units of gamma-ray fluxes (F_1 and F_2) are in 10^{-7} ph cm^{-2} s^{-1} and X-rays/Optical/UV are is units of 10^{-11} erg cm^{-2} s^{-1}.

3.2. γ-Ray Variability

During 2015, the source was very active as had been also seen earlier. The maximum flux attained at this time is $(5.50 \pm 0.34)\times10^{-6}$ ph cm^{-2} s^{-1} with photon spectral index 1.86 at MJD 57244.5. The variability of the source can be seen from the gamma-ray light curve in Figure 1, which represents all the flares along with the photon spectral index in the second panel.

It is seen that as the flux increases in gamma-ray the photon spectral index becomes harder and harder. The flux doubling/halving time is estimated during the flaring episodes by using the following equation (Brown 2013; Saito et al. 2013; Paliya 2015):

$$F_2 = F_1 2^{(t_2-t_1)/\tau_d}, \quad (1)$$

where F_1 and F_2 are the fluxes measured at two consecutive times t_1 and t_2, and τ_d represents the doubling/halving timescale. One day binned gamma-ray light curve, shown in Figure 1, revealed the flux doubling time of 10.6 hr, when the source flux is changing from 1.15×10^{-6} to 5.50×10^{-6} between MJD 57243.5 and MJD 57244.5.

3.3. X-Ray Variability

The source is also followed by the *Swift*-XRT/UVOT telescope to unveil the behavior in X-ray, UV, and optical bands. In the third panel of Figure 1, we have shown the X-ray light curve in the energy range of 0.3–10 keV. The X-ray light curve is scanned by Equation (1) and the flux doubling time is estimated for the consecutive time interval and it is found that the source is less variable in X-rays, moreover flaring states cannot be clearly identified. The flux doubling time estimated by using Equation (1) from the X-ray light curve is 2.5 days for $F_1 = 1.38 \times 10^{-11}$ erg cm^{-2} s^{-1} at t_1 = MJD 57156.41 and $F_2 = 1.07 \times 10^{-11}$ erg cm^{-2} s^{-1} at t_2 = MJD 57157.34.

3.4. Optical and UV Variability

The *Swift*-UVOT light curve is plotted in the fourth and fifth panels of Figure 1. The source variability is significant during flare C while flares A, B, and D are less variable. In these three flares (A, B, and D) the variability of the source is constrained by the number of observations. Equation (1) applied to the entire light curve of optical and *UV* band and the flux doubling times estimated for *U*, *B*, and *V* band light curves are 1.0, 0.7, and 1.1 days respectively (see Table 1). Similar behavior has also been seen in *UV* band (*W1*, *M2*, *W2*). The flux doubling times estimated in these three bands of *UV* (*W1*, *M2*, *W2*) are 0.8, 1.4, and 1.1 days.

3.5. Radio Light Curves

The last panel of Figure 1 represents the radio light curve in two different frequencies. OVRO and SMA telescope radio data at 15 and 230 GHz are plotted in the last panel of Figure 1. The radio light curves during 2015 clearly show that the radio fluxes in both the bands are increasing toward the end of the year. The maximum radio flux in 2015 has been recorded as 4.77 Jy and 4.55 Jy at 15 GHz and 230 GHz respectively. The flux doubling time for the radio light curve is not estimated because of the poorly sparse data points.

The fractional variability ($F_{\rm var}$) in different wavebands are also estimated following Vaughan et al. (2003). For the gamma-ray light curve $F_{\rm var}$ is found to be 1.04 ± 0.01, which corresponds to more than 100% variability. The $F_{\rm var}$ estimated for the X-ray light curve is 0.14 ± 0.04, which is the lowest among all the wavebands. A good amount of fractional variability is noticed from the optical light curve shown in Figure 1. The $F_{\rm var}$ in optical *U*, *B*, and *V* bands is found to be 0.55 ± 0.01, 0.59 ± 0.01, and 0.64 ± 0.01 respectively, and in *UV* bands for *W1*, *M2*, and *W2* filters it is found to be 0.56 ± 0.01, 0.53 ± 0.01, and 0.48 ± 0.01. The fractional variability is also computed for the radio light curve at 15 and 230 GHz. From the OVRO light curve at 15 GHz the $F_{\rm var}$ is found to be 0.34 ± 0.01. The SMA light curve shown in Figure 1 shows the large fractional variability compared to the OVRO light curve and the $F_{\rm var}$ is noticed as 0.60 ± 0.02.

3.6. Cross-correlation

A cross-correlation study between different energy bands can be done to find out the location of different emission regions responsible for multiwavelength emission along the jet axis. The discrete correlation function (DCF) formulated by Edelson & Krolik (1988) can be used to estimate cross and auto-correlations of the unevenly sampled light curves. We have made a few different combinations to show the DCFs. The combinations are γ-*Swift B* band, γ-X-rays, γ-OVRO, γ-SMA, and OVRO-SMA. DCFs for all these combinations are shown in Figure 2. When the two light curves LC1 and LC2 are cross-correlated, a positive time lag between them implies that the light curve LC1 is leading with respect to LC2, and a negative time lag implies the opposite.

γ-ray versus optical B-band DCF: The left most plot of Figure 2 (upper panel) shows the DCF between γ-ray and *Swift* optical *B*-band, and it is found that there are different peaks at different time lags. We select the peak near zero time lag to constrain the location of the emission region. The peaks at +52 days and −20 days and the other two outer peaks could be due to a strong gamma-ray flare correlating with a strong optical flare within the total period used for DCF analysis. A peak is observed at a time lag of 3.9 days, though the correlation coefficient is not very significant. We have estimated the average time resolution of the worst light curve and the DCF time bin is chosen as three times the average time resolution (Edelson & Krolik 1988; Castignani et al. 2014). In case of gamma-ray versus optical *B*-band the DCF time bin is

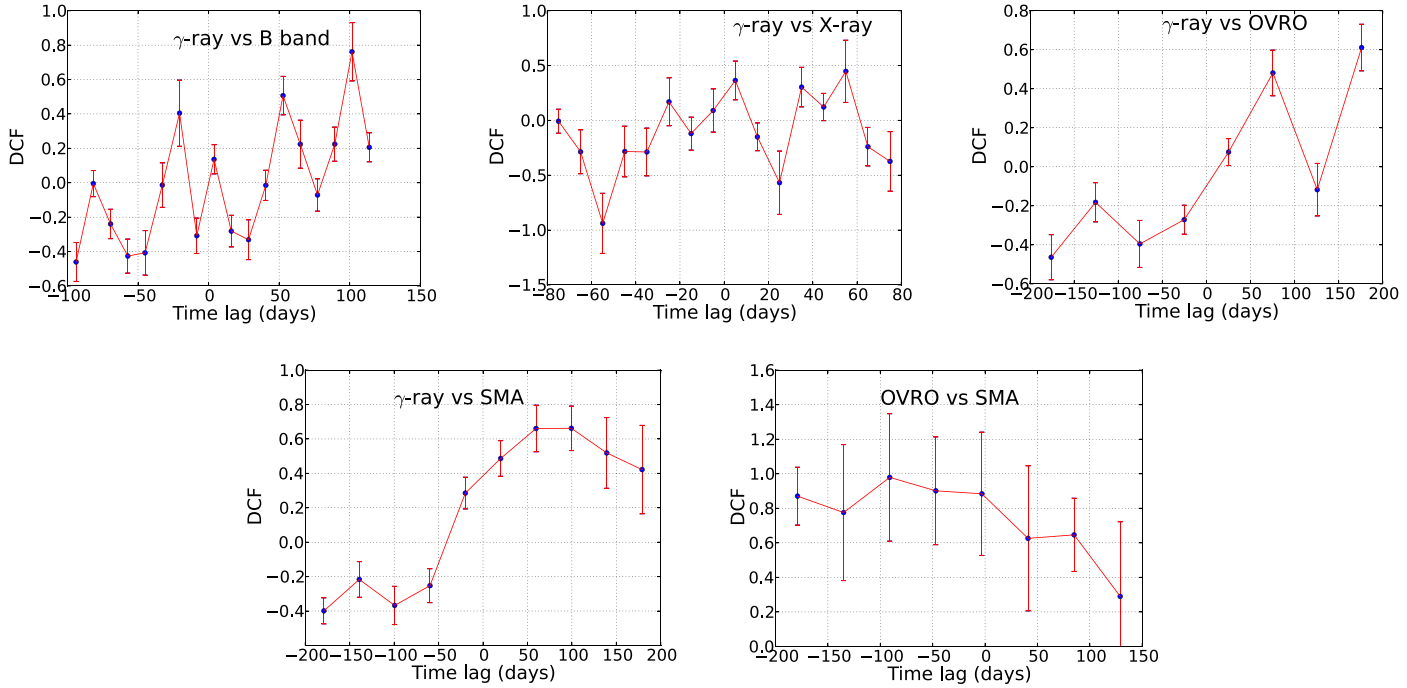

Figure 2. DCFs for different combinations are plotted from top to bottom. The meanings of positive and negative time lags are described in Section 3.6.

12.2 days. The peak found within the DCF time bin is not considered as a time lag. The multiple peaks in DCF are also observed by Kushwaha et al. (2017) for 3C 454.3 during segment 4 as mentioned in their paper. The zero time lag observed by Castignani et al. (2017) for PKS 1510-089 and the small time lag observed in our case are consistent with the results obtained by Abdo et al. (2010) and Nalewajko et al. (2012) for other epochs. A zero or small time lag between two different emissions suggests their cospatial origin. Similar results were also found for different sources (Kaur & Baliyan 2018; Prince 2019). The inference of a small time lag between gamma-ray and optical *B* band emission has been used to assume that the gamma-ray and optical photons are produced in the same region by the inverse Compton (IC) and synchrotron emission of the same population of electrons respectively.

γ-ray versus X-ray DCF: The gamma-ray versus X-ray DCF is shown in the middle plot of the upper panel of Figure 2. A peak is observed at time lag 4.99 days with a correlation coefficient 0.36 ± 0.17. The DCF time bin 10.2 days is chosen on the basis of the average time resolution of the X-ray light curve. The observed peak is within the DCF time bin and hence is not considered as the time lag between gamma-ray and X-ray emission. The peak observed at the edge of the DCF can be discarded. A time lag of 50 days between gamma-rays and X-rays has been seen by Castignani et al. (2017) in PKS 1510-089. This time lag between gamma-rays and X-rays suggests that the X-rays might have been produced far away from the region of gamma-ray emission in the jet. A small correlation coefficient found in our case makes our results consistent with the result obtained by Abdo et al. (2010), where they have also not found any robust evidence of cross-correlation between gamma-ray and X-ray at zero time lag.

γ-ray versus OVRO and SMA DCF: The rightmost plot of the upper panel and left plot of the lower panel of Figure 2 represent the gamma-ray versus OVRO (15 GHz) and gamma-ray versus SMA (230 GHz) DCFs respectively. In gamma-ray versus OVRO, a peak is observed at time lag 75 days, which is almost equal to one-third of the length of the OVRO light curve. Hence, it cannot be considered as a DCF peak. Similar behavior is also seen in gamma-ray versus SMA DCF, where a peak is observed at the time lag between 60 and 100 days. This peak also lies at one-third of the length of the SMA light curve and hence cannot be considered as a DCF peak.

OVRO versus SMA DCF: We have also tried to estimate the DCF between OVRO (15 GHz) and SMA (230 GHz) and the result is shown in the lower panel of Figure 2. The DCF analysis does not show any significant peak, hence it is difficult to comment anything about the correlation between these two emissions.

From the DCF analysis, it is clear that no good correlation is observed in any of the pairs. One of the reasons behind this is the nonavailability of good quality data and a significant number of observations in X-ray, optical, and radio wavelengths for this particular time period. Hence, it would not be justified to conclude anything about the locations of different emission regions from this analysis.

3.7. Multiwavelength SED Modeling with GAMERA

Our analysis shows that the source went in long and bright flaring episodes in 2015. The four bright flares are identified as Flare-A, Flare-B, Flare-C, and Flare-D. The quiescent states (Q1 and Q3) were observed before and after the flares and the quiescent state Q2 in between Flare-B and Flare-C. We have produced the gamma-ray SED in the energy range 0.1–300 GeV, for all four gamma-ray flares along with one of the quiescent states Q2, by using the unbinned likelihood analysis. The observed gamma-ray spectrum are fitted with four different functional forms PL, Log Parabola (LP), Broken Power Law and PL with Exponential cut-off (PLEC) as discussed in Prince et al. (2018). We have found that the gamma-ray SED data points for

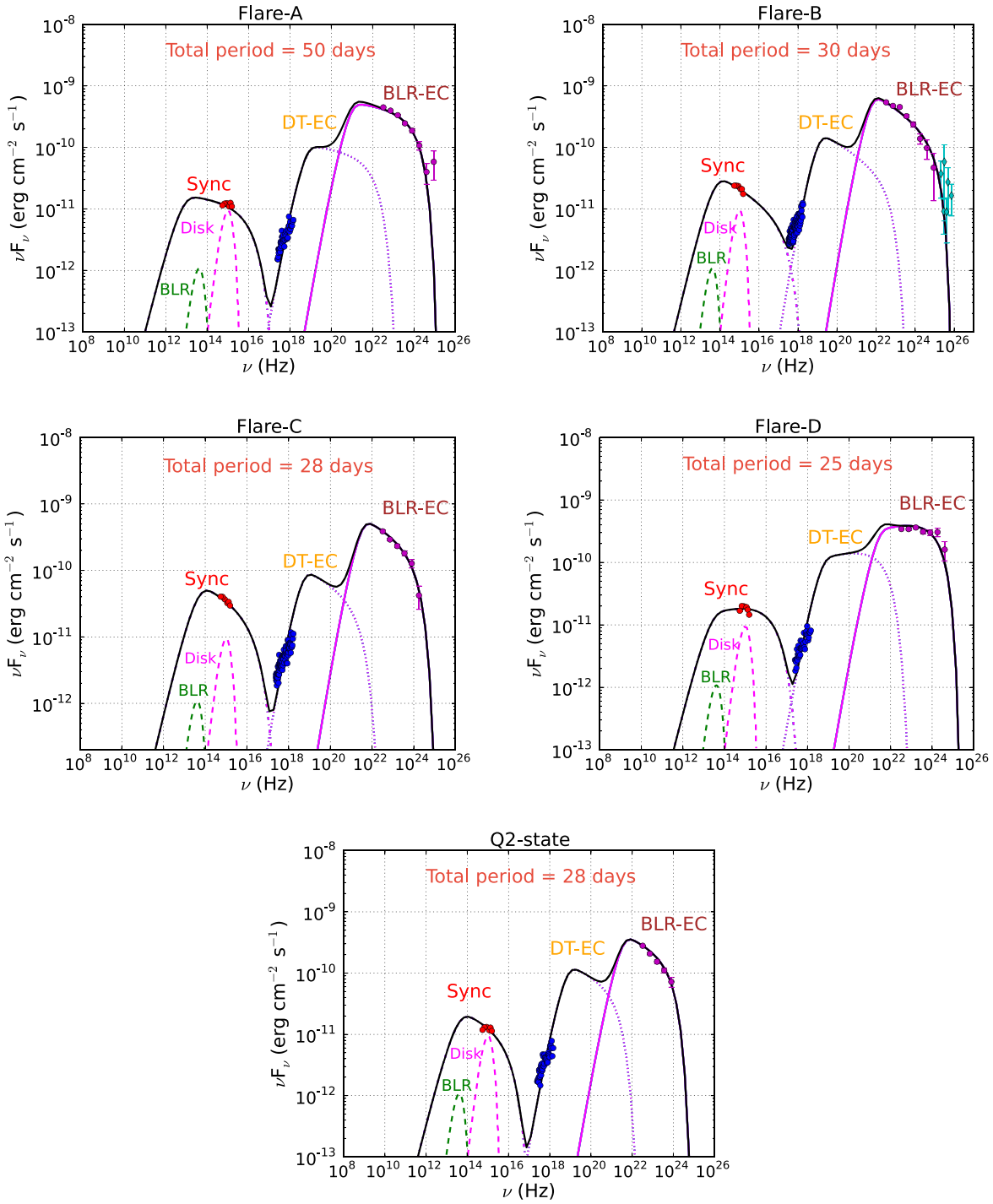

Figure 3. Multiwavelength SED modeling for four flares and quiescent state Q2. *Swift*-XRT/UVOT data points shown in blue/red solid circles. *Fermi*-LAT data points are shown with pink solid circles, for Flare B the deabsorbed MAGIC data points (Ahnen et al. 2017) are shown with teal diamonds.

all the flares and state Q2 are well described by the LP distribution function. An LP photon spectrum can be produced by radiative losses of an LP electron spectrum (Massaro et al. 2004). Due to this reason we have considered LP distribution for the injected electron spectrum in our multiwavelength SED modeling. In X-rays and UV/Optical, the SED data points are also produced. All the spectral data points are plotted together in Figure 3 and modeled using the publicly available code GAMERA[6] (Prince et al. 2018). GAMERA solves the time-dependent transport equation for input injected electron spectrum, and it calculates the propagated electron spectrum, and further, it uses this propagated electron spectrum as an input and estimates the synchrotron, synchrotron self-Compton (SSC), and IC emission.

The following continuity equation we have used in our study:

$$\frac{\partial N(E,t)}{\partial t} = Q(E,t) - \frac{\partial}{\partial E}(b(E,t)N(E,t)), \qquad (2)$$

[6] http://libgamera.github.io/GAMERA/docs/main_page.html

$Q(E, t)$ is the injected electron (electron and positron) spectrum, $N(E, t)$ is the propagated electron spectrum after the radiative loss, and $b(E, t)$ covers the energy loss rate of electrons due to the synchrotron, SSC, and EC emission. The code GAMERA estimates the IC emission using the full Klein–Nishina cross-section from Blumenthal & Gould (1970).

The flux doubling times (see Table 1) estimated in different wavelengths suggest different emission zones. The doubling times found in gamma-ray and UV/Optical bands are closer to each other, which suggests they might have been produced in the same region. Two emission regions are considered in this work, one is responsible for optical/UV and gamma-ray emission and another for the X-ray emission.

The locations of the emitting blobs along the jet axis are estimated by using the flux doubling timescales. We have used the following relation:

$$d = \frac{ct_d\delta}{(1+z)\theta_{\rm jet}}, \tag{3}$$

where t_d is the flux doubling time and $\theta_{\rm jet}$ is the half opening angle of the jet (Kaur & Baliyan 2018), d is the distance of the emitting region from the central supermassive black holes (SMBH), c is the speed of light in vacuum, $z = 0.361$ is the redshift of the source, and $\delta = 25$ is the Doppler factor. The jet opening angle was estimated from the radio observations by using the relation $\theta_{\rm jet} = \theta_p \sin\langle\Theta_0\rangle$, where $\theta_p = 4.8°$ is the projected half opening angle, and $\langle\Theta_0\rangle$ is the angle between jet axis and the line of sight. With the values of θ_p and $\langle\Theta_0\rangle$ from Jorstad et al. (2005) the jet opening angle is found to be $0\overset{\circ}{.}12$. The observed flux doubling times for gamma-rays and X-rays are 10.6 hr and 2.5 days, respectively, which are used to estimate the distances of the emission regions by using Equation (3). The distance of the gamma-ray emitting blob from the central SMBH is estimated at 1.76×10^{17} cm and the location of the X-ray emitting blob is estimated as 1.0×10^{18} cm along the jet axis. The exact boundary of the BLR is not known, but we have some idea about the radius of the BLR. To estimate the size of BLR and DT, a simple scaling law is given by Ghisellini & Tavecchio (2009). It only depends on the disk luminosity ($L_{\rm disk}$). The relations are $R_{\rm BLR} = 10^{17} L_{d,45}^{1/2}$ and $R_{\rm DT} = 2.5 \times 10^{18} L_{d,45}^{1/2}$, where $L_{d,45}$ is the disk luminosity in units of $10^{45}\,{\rm erg\,s^{-1}}$. The disk luminosity was estimated earlier by several authors (Celotti et al. 1997; Nalewajko et al. 2012) in the range of $3–7 \times 10^{45}\,{\rm erg\,s^{-1}}$. Using the typical value of disk luminosity ($L_{\rm disk} = 6.7 \times 10^{45}\,{\rm erg\,s^{-1}}$), we have found that the radius of BLR ($R_{\rm BLR}$) is 2.6×10^{17} cm and the size of the DT ($R_{\rm DT}$) region is 6.47×10^{18} cm. From this calculation we conclude that the gamma-ray emitting blob is located within the edge of the BLR whereas the X-ray emitting blob lies outside the BLR, in the DT region. We use these inferences in the SED modeling with the time dependent code GAMERA.

All the different flares and quiescent state Q2 are modeled with GAMERA as shown in Figure 3. The model parameters are presented in Table 2. The energy density of the external radiation field in the comoving jet frame is given as

$$U'_{\rm ext} = \frac{\Gamma^2 \xi_{\rm ext} L_{\rm disk}}{4\pi c R_{\rm ext}^2}, \tag{4}$$

where "ext" represents the BLR or DT. The values of $\xi_{\rm BLR} = 0.06$, and $\xi_{\rm DT} = 0.12$ are comparable to Barnacka et al. (2014) and the jet Lorentz factor $\Gamma = 20$, taken from Aleksić et al. (2014). Using Equation (4), the BLR energy

Table 2
Parameters of Two Zone Modeling, Injection Spectrum of Electrons $dQ(E)/dE = Q_p\,(E/E_p)^{-\alpha-\beta\log(E/E_p)}$, $E_p = 90$ MeV

Model Parameters	BLR	DT
Energy density in BLR/DT (erg cm^{-3})	6.41	0.002
Temperature in BLR/DT (K)	1e4	1e3
Doppler factor (δ)	25	25
Lorentz factor (Γ)	20	20
Size of blob ($r_{\rm blob}$ cm)	2.1×10^{16}	1.2×10^{17}
Flare-A		
Jet power in electrons (P_e erg s^{-1})	1.15×10^{45}	8.79×10^{44}
Jet power in magnetic field (P_B erg s^{-1})	5.18×10^{45}	2.16×10^{42}
Injected electron spectrum (α)	2.0	3.1
β	0.08	0.08
$\gamma_{\rm min}$	100	25
$\gamma_{\rm max}$	9×10^3	2.2×10^3
Magnetic field (B Gauss)	2.8	0.01
Flare-B		
Jet power in electrons (P_e erg s^{-1})	1.08×10^{45}	1.67×10^{45}
Jet power in magnetic field (P_B erg s^{-1})	8.10×10^{45}	2.16×10^{42}
Injected electron spectrum (α)	2.1	3.3
β	0.16	0.08
$\gamma_{\rm min}$	250	30
$\gamma_{\rm max}$	2.7×10^4	4×10^3
Magnetic field (B Gauss)	3.5	0.01
Flare-C		
Jet power in electrons (P_e erg s^{-1})	9.38×10^{44}	1.30×10^{45}
Jet power in magnetic field (P_B erg s^{-1})	1.72×10^{46}	2.16×10^{42}
Injected electron spectrum (α)	2.1	3.5
β	0.17	0.10
$\gamma_{\rm min}$	190	24
$\gamma_{\rm max}$	8×10^3	9×10^2
Magnetic field (B Gauss)	5.1	0.01
Flare-D		
Jet power in electrons (P_e erg s^{-1})	8.27×10^{44}	2.51×10^{44}
Jet power in magnetic field (P_B erg s^{-1})	7.65×10^{45}	2.16×10^{42}
Injected electron spectrum (α)	1.7	3.0
β	0.07	0.07
$\gamma_{\rm min}$	170	25
$\gamma_{\rm max}$	1.2×10^4	1.3×10^3
Magnetic field (B Gauss)	3.4	0.01
Quiescent State (Q2)		
Jet power in electrons (P_e erg s^{-1})	7.80×10^{44}	1.63×10^{45}
Jet power in magnetic field (P_B erg s^{-1})	9.55×10^{45}	2.16×10^{42}
Injected electron spectrum (α)	2.2	3.3
β	0.08	0.08
$\gamma_{\rm min}$	200	27
$\gamma_{\rm max}$	6×10^3	8×10^2
Magnetic field (B Gauss)	3.8	0.01

density in the jet comoving frame is estimated as $U'_{\rm BLR} = 6.41$ erg cm^{-3} and DT energy density as $U'_{\rm DT} = 2 \times 10^{-3}$ erg cm^{-3}. The temperature of the BLR is used from Peterson (2006), $T_{\rm BLR} = 10^4$ K and the temperature of the DT region, $T_{\rm DT} = 10^3$ K from Ahnen et al. (2017).

The Doppler factor (δ) and Lorentz factor (Γ) for PKS 1510-089 have been chosen from an earlier study by Aleksić et al. (2014). The sizes of the gamma-ray and X-ray emitting blobs are estimated by the relation $R < c\tau_d\ \delta/(1+z)$, where τ_d denotes the doubling time in two different bands. The sizes of the emitting blobs are found to be 2.1×10^{16} cm and 1.2×10^{17} cm for gamma-ray and X-ray emission respectively.

The electron spectra for all the flares and the quiescent state evolve with time as the electrons lose energy radiatively by synchrotron and IC emission. The duration of each flare and the quiescent state are significantly longer than the cooling timescale of electrons, as a result the electron spectra become steady in a short time. The total time duration of flares A, B, C, and D are 50 days, 30 days, 28 days, and 25 days, respectively, and the quiescent state Q2 lasted for 28 days. The synchrotron emission depends on the strength of the magnetic field and the luminosity of the relativistic electrons. The EC emission depends on the energy density and temperature of the external photons and also the luminosity of the relativistic electrons. The synchrotron self-Compton (SSC) emission depends on the energy density of the synchrotron photons, which depends on the size of the blob, magnetic field, and luminosity of the relativistic electrons. The SSC emission is found to be very low in our model compared to the EC emission. For the given magnetic field in the DT region the synchrotron emission is found to be below 10^{-13} erg cm^{-2} s^{-1}, hence not visible in Figure 3.

The optical depth correction due to the absorption of gamma-rays by the EBL (extragalactic background light) is not important for the *Fermi*-LAT observed gamma-ray flux from PKS 1510-089. We have included the optical depth correction on the observed data points by MAGIC from Ahnen et al. (2017). The deabsorbed data points are used in the SED modeling. To obtain the best model fit to the data points we have optimized the following parameters, e.g., the magnetic field in the blob, luminosity, and spectral index of injected relativistic electrons, and also their minimum and maximum energies ($\gamma_{\rm min}$, $\gamma_{\rm max}$).

We have assumed the ratio of pairs (electrons and positrons) to cold protons in the emission regions is 10:1. The jet power in the relativistic electrons and positrons, or the magnetic field, or the cold protons is calculated with this expression $P_{e,B,p} = \pi\ r_{\rm blob}^2\ \Gamma^2\ c\ U_{e,B,p}$, where $U_{e,B,p}$ denotes the energy density in electrons and positrons, or magnetic field, or cold protons. The total jet power is always found to be lower than the Eddington's luminosity of the source 6.86×10^{46} erg s^{-1}, calculated with the black hole mass given in Abdo et al. (2010). The parameter values which can explain the SEDs of flares A, B, C, and D, and the quiescent state Q2 are listed in Table 2.

4. Discussion

Below we discuss our results and compare them with those of previous work.

4.1. Multiwavelength Studies with SED Modeling

The flaring states identified as A, B, C, and D and the quiescent states Q1, Q2, and Q3 are shown in the gamma-ray light curve in Figure 1 along with the light curves in other wavelengths. The flux doubling times in different wavelengths are found to be different, which motivated us to fit the SED with a two-zone model. The values of the parameters used in two zone modeling are displayed in Table 2. The magnetic field in the first zone required to fit the optical and UV data points is in the range of 2.8–5.1 Gauss. This emission zone is located near the outer boundary of the BLR region. The magnetic field in the second zone located in the DT region is not constrained by optical or UV data in our model. It is assumed to be very low to minimize the jet power. However, in principle, it could be higher. The X-ray flux constrains the jet power in electrons and positrons in the second zone. In the first zone the magnetic field has more jet power than that in electrons and positrons. In this zone the electrons and positrons carry more energy during the flaring states. MAGIC detected very high energy gamma-rays (Ahnen et al. 2017) during Flare B. The maximum energy of the relativistic electrons and positrons in our model is the highest during flare B. In the second zone also this jet power is expected to be higher during the flaring states if the X-ray flux is higher than that in the quiescent states.

Abdo et al. (2010) noted a complex correlation between fluxes in different wavelengths during the flaring activity of PKS 1510-089 between 2008 September and 2009 June. The high state of PKS1510-089 in 2009 was also studied by Marscher et al. (2010). They found that the gamma-ray peaks were simultaneous with maxima in optical flux.

The 2009 GeV flares of PKS 1510-089 have been studied by Dotson et al. (2015). They have discussed the location of these flares. For two flares they have suggested that the emission region is at the DT region and for the other two at the vicinity of VLBI radio core. Barnacka et al. (2014) modeled the high energy flares detected in 2009 March from PKS 1510-089. They have used the photons in the BLR and DT regions for EC emission to model the flares. SSC emission is insignificant in their model. In their model the emission zone is located at a distance of 7×10^{17} cm from the black hole.

The low states of this source between 2012 and 2017 have been studied in detail recently using MAGIC data (MAGIC Collaboration; Acciari et al. 2018). Their analysis shows that the location of the gamma-ray emission region is close to the outer edge of the BLR region. They have chosen two scenarios with the emission regions located at 7×10^{17} cm and 3×10^{18} cm away from the black hole respectively. For the high state in 2015 Ahnen et al. (2017) located the emission region at 6×10^{17} cm away from the black hole. These estimates are comparable to our results. In their work, the gamma-ray emission region has a size of 2.8×10^{16} cm, which is also comparable to the size of the gamma-ray emission region found in our study 2.1×10^{16} cm. Our Lorentz factor and Doppler factor values are similar to those of Aleksić et al. (2014).

The light curves of PKS 1510-089 and 3C 454.3 were studied by Tavecchio et al. (2010) for the period from 2008 August 4 to 2010 January 31 to constrain the location of the emission region through rapid variability in gamma-rays in the *Fermi*-LAT data. From hour scale variability in gamma-ray flux they constrained the size of the emission region to be less than 4.8×10^{15} cm and 3.5×10^{15} cm for PKS 1510-089 and

3C 454.3, respectively, for Doppler factor $\delta = 10$. The extreme value of Doppler factor $\delta = 50$ constrains the size of the emission region to less than 0.01 pc. They suggested that such small emission regions are likely to be located near the black hole. They concluded that the far dissipation scenario, where the gamma-ray emission region is located 10–20 pc away from the black hole is disfavored.

A time dependent modeling of gamma-ray flares of PKS 1510-089 has been carried out by Saito et al. (2015) within the framework of the internal shock scenario. They have shown that the emission region is located between 0.3 and 3 pc from the black hole depending on whether the jet is freely expanding or collimated. They have discussed nonuniformity of the Doppler factor across the jet due to the radial expansion of the outflow. This may result in time distortion in the observed gamma-ray light curve, in particular, asymmetric flux profiles with extended decay times.

The most variable blazar 3C 454.3 has been well studied and modeled with multiwavelength observations (Finke 2016). Multiwavelength temporal variability in 3C 454.3 during its active state in 2014 has been studied by Kushwaha et al. (2017). They found in some of the epochs IR/optical and gamma-ray fluxes show nearly simultaneous variation. Correlation in optical and gamma-ray frequencies was observed in 2016 June outburst of 3C 454.3 (Weaver et al. 2019). Recently, Rajput et al. (2019) analyzed quasi-simultaneous data at optical, UV, X-ray, and gamma-ray energies collected over a period of 9 years, 2008 August to 2017 February. They identified four epochs when the source showed large optical flares. The optical and gamma-ray flares are correlated in two epochs. In two other epochs the flares in gamma-rays are weak or absent.

A correlation in optical and gamma-ray photons from flares of PKS 1510-089 during 2009 January to 2010 January has been suggested by Castignani et al. (2017), which could be a common feature among these blazars. This inference has also been used in our analysis to model the SEDs. We also note that in some FSRQs like 3C 279 the time lag between optical and gamma-ray emission could be due to the variations in the ratio of energy densities in external photon field and magnetic field with distance across the length of the jet (Janiak et al. 2012).

4.2. Gamma–Radio Correlation

An interesting feature of these flares is the gradual increase in the radio flux over a long period of time. In the bottom panel of our Figure 1, the light curves at 15 GHz from OVRO observations and at 230 GHz from SMA observations are shown. DCF estimated between these two light curves does not show any clear peak or lag in Figure 2. Even at the end of the high state when the gamma-ray flux reached the quiescent state Q3 the radio flux continued to increase. The OVRO flux reached the maximum level in 2016 October and subsequently decreased slowly.

Ahnen et al. (2017) also reported gradual increase in radio flux in the second half of 2015. They have shown the light curve of the radio core at 43 GHz. A bright and slow radio knot K15 was ejected on MJD 57230 ± 52. They associated the increase in radio flux with the ejection of the radio knot K15. Due to the large uncertainty in the ejection time of K15 it could not be associated with any particular GeV flare.

A similar feature was also observed with the gamma-ray high state in 2012 February–April when a radio knot K12 emerged from the core (Aleksić et al. 2014). In the second half of 2011, PKS 1510-089 had a major outburst in radio flux. The outburst first peaked at higher frequency. The peak at 37 GHz was reached around 2011 October 21 and later at 15 GHz around 2011 December 15. After attaining the peaks the light curves gradually decayed. Small outbursts continued to happen after this. VLBA 43 GHz images show a new component (knot K11) in 2011 December. This was also observed at 15 GHz in MOJAVE as reported by Orienti et al. (2013). The temporal evolution of gamma-ray and radio flux suggests they are produced by different populations of electrons, located at different regions along the length of the jet.

5. Conclusions

In this work, the high state of PKS 1510-089 in 2015 has been studied using the gamma-ray data from *Fermi*-LAT, *Swift*-XRT/UVOT and radio data from OVRO and SMA observatory. Four flares are identified as A (MJD 57100 to MJD 57150), B (MJD 57150 to MJD 57180), C (MJD 57208 to MJD 57235), and D (MJD 57235 to MJD 57260) between quiescent states Q1 and Q3. Between flares B and C a quiescent state Q2 (MJD 57180 to MJD 57208) has also been identified. The epochs of MAGIC observations of flares in 2015 are within the duration of our flare B. We have also included MAGIC data for this flare from Ahnen et al. (2017). We have inferred about the locations of the emission regions in different wavelengths from the flux doubling timescales. It is found that the source is less variable in X-rays and the flaring states cannot be clearly identified. In our work the optical and gamma-ray emission is assumed to be cospatial. This region of emission is located within the edge of the BLR region and the X-ray emission could be from the DT region. The modeling has been done with the publicly available time dependent code GAMERA considering two emission zones. An LP distribution of injected electrons is propagated using the code GAMERA and subsequently, the synchrotron, EC, and SSC emission has been calculated to fit the observed data. The parameter values used in our two zone model are displayed in Table 2. The data could be adequately fitted by adjusting the injected electron spectrum and the magnetic field. The jet power required in this scenario is below the Eddington's luminosity of PKS 1510-089.

The authors thank the referee for fruitful comments that improved this paper. This work has made use of publicly available *Fermi*-LAT data from FSSC and XRT data analysis software (XRTDAS) developed by ASI science data center, Italy. Archival data from the SMA observatory and from the OVRO 40 m monitoring program (Richards et al. 2011) have also been used in this research. N.G. acknowledges the hospitality of the Nicolaus Copernicus Astronomical Center. This work was partially supported by the Polish National Science Centre grant 2015/18/E/ST9/00580.

ORCID iDs

Raj Prince https://orcid.org/0000-0002-1173-7310
Krzysztof Nalewajko https://orcid.org/0000-0002-2019-9438

References

Abdo, A. A., Ackermann, M., Agudo, I., et al. 2010, ApJ, 721, 1425
Abramowski, A., Acero, F., Aharonian, F., et al. 2013, A&A, 554, A107
Acciari, V. A., Ansoldi, S., Antonelli, L. A., et al. 2018, A&A, 619, A159

Acero, F., Ackermann, M., Ajello, M., et al. 2015, ApJS, 218, 23
Ahnen, M. L., Ansoldi, S., Antonelli, L. A., et al. 2017, A&A, 603, A29
Aleksić, J., Ansoldi, S., Antonelli, L. A., et al. 2014, A&A, 569, A46
Atwood, W. B., Abdo, A. A., Ackermann, M., et al. 2009, ApJ, 697, 1071
Barnacka, A., Moderski, R., Behera, B., Brun, P., & Wagner, S. 2014, A&A, 567, A113
Basumallick, P. P., & Gupta, N. 2016, APh, 88, 1
Blumenthal, R., & Gould, G. 1970, RvMPh, 42, 237
Böttcher, M., Reimer, A., Sweeney, K., & Prakash, A. 2013, ApJ, 768, 54
Breeveld, A. A., Landsman, W., Holland, S. T., et al. 2011, in AIP Conf. Proc. 1358, GAMMA RAY BURSTS 2010, ed. J. E. McEnery, J. L. Racusin, & N. Gehrels (Melville, NY: AIP), 373
Brown, A. 2013, MNRAS, 431, 824
Castignani, G., Guetta, D., Pian, E., et al. 2014, A&A, 565, A60
Castignani, G., Pian, E., Belloni, T. M., et al. 2017, A&A, 601, A30
Celotti, A., Padovani, P., & Ghisellini, G. 1997, MNRAS, 286, 415
Dotson, A., Georganopoulos, M., Meyer, E., & McCann, K. 2015, ApJ, 809, 164
Edelson, R. A., & Krolik, J. H. 1988, ApJ, 333, 646
Finke, J. D. 2016, ApJ, 830, 94
Fossati, G., Celotti, A., Chiaberge, M., et al. 2000, ApJ, 541, 153
Ghisellini, G., & Tavecchio, F. 2009, MNRAS, 397, 985
Gurwell, M. A., Peck, A. B., Hostler, S. R., Darrah, M. R., & Katz, C. A. 2007, in ASP Conf. Ser. 375, From Z-Machines to ALMA: (Sub)Millimeter Spectroscopy of Galaxies, ed. A. J. Baker et al. (San Francisco, CA: ASP), 234
Janiak, M., Sikora, M., Nalewajko, K., Moderski, R., & Madejski, G. M. 2012, ApJ, 760, 129
Jorstad, S. G., Marscher, A. P., Lister, M. L., et al. 2005, AJ, 130, 1418
Kalberla, P. M. W., Burton, W. B., Hartmann, D., et al. 2005, A&A, 440, 775
Kataoka, J., Madejski, G., Sikora, M., et al. 2008, ApJ, 672, 787
Kaur, N., & Baliyan, K. S. 2018, A&A, 617, 59
Kushwaha, P., Gupta, A. C., Misra, R., & Singh, K. P. 2017, MNRAS, 464, 2046
Larionov, V. M., Villata, M., Raiteri, C. M., et al. 2016, MNRAS, 461, 3047
Marscher, A. P., Jorstad, S., Larionov, V., et al. 2010, ApJL, 710, L126
Massaro, E., Perri, M., Giomi, P., & Nesci, R. 2004, A&A, 413, 489
Nalewajko, K. 2013, MNRAS, 430, 1324
Nalewajko, K., Sikora, M., Madejeski, G., et al. 2012, ApJ, 760, 69
Orienti, M. D., Ammando, F., Giroletti, M., et al. 2013, MNRAS, 428, 2418
Paliya, V. S. 2015, ApJL, 808, L48
Peterson, B. M. 2006, in Physics of Active Galactic Nuclei at all Scales, ed. D. Alloin (Berlin: Springer), 77
Prince, R. 2019, ApJ, 871, 101
Prince, R., Majumdar, P., & Gupta, N. 2017, ApJ, 844, 62
Prince, R., Raman, G., Hahn, J., Gupta, N., & Majumdar, P. 2018, ApJ, 866, 16
Rajput, B., Stalin, C. S., Sahayanathan, S., Rakshit, S., & Mandal, A. K. 2019, MNRAS, 486, 1781
Richards, J. L., Max-Moerbeck, W., Pavlidou, V., et al. 2011, ApJS, 194, 29
Roming, P. W. A., Kennedy, T. E., Mason, K., et al. 2005, SSRv, 120, 95
Saito, S., Stawarz, L., Tanaka, Y. T., et al. 2015, ApJ, 809, 171
Saito, S., Stawarz, L., Tanaka, Y. T., et al. 2013, ApJL, 766, L11
Schlafly, E. F., & Finkbeiner, D. P. 2011, ApJ, 737, 103
Tanner, A. M., Bechtold, J., Walker, C. E., Black, J. H., & Cutri, R. M. 1996, AJ, 112, 62
Tavecchio, F., Ghisellini, G., Bonnoli, G., & Ghirlanda, G. 2010, MNRAS, 405, L94
Vaughan, S., Edelson, R., Warwick, R. S., & Uttley, P. 2003, MNRAS, 345, 1271
Weaver, Z. R., Balonek, T. J., Jorstad, S. G., et al. 2019, ApJ, 875, 15
Zacharias, M., Böttcher, M., Chakraborty, N., et al. 2016, in AIP Conf. Proc. 1792, HIGH ENERGY GAMMA-RAY ASTRONOMY: 6th International Meeting on High Energy Gamma-Ray Astronomy, ed. A. Aharonian, W. Hofmann, & F. M. Rieger (Melville, NY: AIP), 05002